nature communications

Article

https://doi.org/10.1038/s41467-025-59520-9

Far-field femtosecond laser-driven λ/73 super-resolution fabrication of 2D van der Waals $NbOI_2$ nanostructures in ambient air

Received: 2 June 2024

Accepted: 22 April 2025

Published online: 04 May 2025

Check for updates

Yanchao Guan[1,2,8], Ye Ding[1,2,3,8], Yuqiang Fang[4] ✉, Jingyi Li[1], Yanan Liu[5], Rui Wang[2,6], Juanyuan Hao[6], Hui Xie[1], Chengyan Xu[6,7], Liang Zhen[6,7], Yang Li[2,6] ✉ & Lijun Yang[1,2,5] ✉

The design and fabrication of ultrafine nanostructures in two-dimensional (2D) van der Waals materials are crucial for the functionalization of electronic devices. Here, we report the utilization of far-field femtosecond laser patterning to fabricate super-resolution nano-groove array (NGA) structures in 2D multilayer $NbOI_2$ in ambient air, achieving groove widths as low as ~14.5 nm (~λ/73). The NGA structures maintain a well-defined single-crystal $NbOI_2$ with amorphous Nb_2O_5 edges as narrow as 3.2 nm. The formation mechanism of NGA structure is confirmed to be associated with the coupled field of surface plasmon polariton periodic field and nano-groove-induced local near-field induced by femtosecond laser irradiation. Furthermore, the NGA-$NbOI_2$ gas sensor exhibits NO_2 sensing performance, with a rapid response time (5.1 s), which is attributed to the existence of abundant $NbOI_2$-Nb_2O_5 heterojunctions. This approach will propel the further development of nano-lithography techniques for functional device applications of 2D materials.

The design and fabrication of ultrafine nanostructure patterning of 2D materials holds crucial significance for the creation of innovative functional architectures[1], integration of electronic devices[2], and advancements in nanophotonics[3]. Nanostructures with dimensions smaller than 100 nm often exhibit unique functionalities in fields such as sensing[4], catalysis[5], and optoelectronics[6]. Various nano-patterning techniques have been developed, including focused ion beam (FIB) lithography[7–9], electron beam lithography (EBL)[10] combined with ion etching, and scanning probe lithography (SPL)[11]. However, these methods often entail high costs and complex operational procedures. FIB requires high-vacuum conditions, while EBL often results in significant residues of photoresist, impacting device performance. Additionally, SPL often struggles to achieve large-area structure fabrication. Therefore, the development of a rapid, efficient, and flexible nanopatterning method is crucial.

As widely recognized, the limitations of optical diffraction impose constraints on the ultimate size achievable through laser direct writing, typically limited to approximately half a wavelength, thereby hindering the fabrication of ultrafine nanostructures. In recent years, some laser processing methods, such as optical field modulation[12–15] and far-field induced near-field effects[16] have made developments in nanostructure fabrication. However, the intricate design of optical systems and stringent operational conditions have restricted further progress. Alternatively, the laser-induced periodic surface structures (LIPSS) technology has garnered significant attention in recent years. The micro-nano-scale array structures can be fabricated using LIPSS without complex optical systems or

[1]School of Mechatronics Engineering, Harbin Institute of Technology, Harbin, China. [2]Key Laboratory of Micro-systems and Micro-structures Manufacturing, Ministry of Education, Harbin Institute of Technology, Harbin, China. [3]Suzhou Research Institute, Harbin Institute of Technology, Suzhou, China. [4]School of Materials Science and Engineering, Shanghai Jiao Tong University, Shanghai, China. [5]Zhengzhou Research Institute, Harbin Institute of Technology, Zhengzhou, China. [6]School of Materials Science and Engineering, Harbin Institute of Technology, Harbin, China. [7]Sauvage Laboratory for Smart Materials, School of Materials Science and Engineering, Harbin Institute of Technology (Shenzhen), Shenzhen, China. [8]These authors contributed equally: Yanchao Guan, Ye Ding. ✉e-mail: fangyuqiang@sjtu.edu.cn; liyang2018@hit.edu.cn; yljtj@hit.edu.cn

operating environments[17,18]. However, the uncontrollable ablation and damage to materials have constrained its further development for nanostructure fabrication, especially in the field of 2D materials. Zuo et al.[19] conducted LIPSS fabrication on MoS_2, resulting in significant thinning, structural ablation, and a considerable amount of nanoscale particle sputtering. Kim et al.[20] explored the nano-periodic patterning of 2D BP under extreme vacuum conditions in the transmission electron microscope (TEM) chamber, achieving excellent quality nano-periodic patterns. Notably, there remains a need for further exploration on how to utilize the LIPSS method to fabricate regular and orderly nano-array structures in 2D materials in air environments and expand their device applications.

Recently, the 2D $NbOX_2$ (X = Cl, Br, I) family[21,22] has garnered significant attention due to its in-plane anisotropic ferroelectric[23,24], optical properties[19], and piezoelectric sensing characteristics[25]. The nanostructure fabrication on 2D $NbOX_2$ holds promise for further exploration of its distinctive properties. Taking an example of $NbOI_2$, this study employs far-field femtosecond (fs) laser patterning successfully to produce nano-groove array (NGA) structures on 2D multilayer $NbOI_2$ with groove widths as low as ~14.5 nm (~λ/73). The structural characterization shows that the NGA structures retain the pristine $NbOI_2$ single-crystal and exhibit ultrafine amorphous Nb_2O_5 edges. In addition, the generation mechanism and tunability of NGA structures are investigated. Finally, utilizing the abundant nano-grooves and their oxide edge heterojunction structures, gas-sensitive devices for NO_2 detection are fabricated based on NGA structures, demonstrating excellent NO_2 sensing performance.

Results and discussion

Fabrication and characterization of nano-groove array structures

We confirmed the feasibility of fabricating super-resolution NGA structures on 2D $NbOI_2$ using fs laser irradiation. The 2D multilayer $NbOI_2$ nanosheets were mechanically exfoliated and transferred onto a silicon dioxide substrate, followed by scanning with a focused Gaussian beam of an fs laser, generating NGA structures in the laser-scanned area (Fig. 1a, b). For laser irradiation, a linearly polarized infrared fs laser with a wavelength of 1064 nm was utilized. The laser was focused to achieve a spot size of approximately 10 μm in an air environment, with specific optical system and operating parameters as described in Supplementary Fig. 1. When a focused fs laser beam irradiates the material surface, it induces surface light scattering or surface plasmons through interference with the incident laser field, leading to the formation of regular LIPSS structures on the material surface[17,18]. As shown in Fig. 1c, after laser patterning, NGA nanostructures were formed on the $NbOI_2$ nanosheets, oriented perpendicular to the polarization direction of the laser. Notably, in contrast to reported LIPSS processing on bulk material or other 2D materials[19], no apparent material ablation and splashing of melted nanoparticles were observed on the surface of 2D $NbOI_2$ nanosheets, indicating excellent processing quality.

Upon magnification of the NGA structures, as illustrated in Fig. 1d, the depth of nanostructures penetrated the entire nanosheet, with nano-groove width as low as 14.5 nm, approximately 1/73 of the wavelength (1064 nm), which confirms the successful achievement of super-resolution nanostructures through fs laser patterning. Due to the convolution effect of the atomic force microscope tip in extreme nanostructures, accurate characterization of the nano-groove structures is challenging (Supplementary Fig. 2); thus, pseudo-colored scanning electron microscope (SEM) images were used to statistically analyze the spacing and width of nano-grooves (Supplementary Fig. 3). Figure 1e reveals a groove spacing range of approximately 70–300 nm and groove width range of approximately 13–25 nm. Figure 1f and Supplementary Table 1 provide a comparative analysis of the resolution-to-wavelength ratio and the limit width resolution of laser-induced nano-groove structures in recent years, including techniques such as laser direct writing[26], optical field modulation[12,14,15], far-field induced near-field etching[16], and LIPSS[27,28]. This comparison confirms the ultrahigh resolution of NGA nanostructures on 2D $NbOI_2$. Raman spectra (Supplementary Fig. 4) and polarized second harmonic generation (SHG) characterization (Supplementary Fig. 5) confirmed that the NGA structure maintained its pristine crystal structure and non-centrosymmetric properties.

Figure 2 presents transmission electron microscopy (TEM) studies of laser-induced super-resolution NGA nanostructures on 2D $NbOI_2$. Multilayer 2D $NbOI_2$ nanosheets were mechanically transferred onto high-temperature-resistant silicon nitride grids and subsequently patterned using fs laser irradiation. The low-magnification TEM images of obtained $NbOI_2$ NGA structures in Fig. 2a and Supplementary Fig. 6 clearly exhibit uniformly distributed ultra-narrow nano-grooves, with individual nano-grooves analyzed to have an average width of 14.9 nm. The selected area electron diffraction (SAED) patterns exhibit clear single-crystal $NbOI_2$ diffraction spots (Fig. 2c), indicating no damage to the crystal structure during laser irradiation. High-resolution TEM (HRTEM) images, as illustrated in Fig. 2d, e, and f, reveals a clear lattice structure of the $NbOI_2$ regions out of nano-grooves, with an interlayer spacing measured at ≈0.28 nm (Fig. 2f), matching well with the $(1\bar{1}\,2)$ crystal plane in the [201] crystallographic axis direction. Additionally, another set of TEM characterizations of NGA structures corroborated that the orientation of laser-induced nano-grooves is independent of crystal structure (Supplementary Fig. 7).

Moreover, the presence of an amorphous layer at the edges is clearly observed in Fig. 2b, e. Further analysis of the nano-groove edge using fast Fourier transform images reveals the amorphous structure of the edges (Supplementary Fig. 8). Energy-dispersive X-ray spectroscopy (EDX) shows the elemental distribution of Nb, O, and I, confirming the absence of Nb and I elements inside the grooves (with unavoidable O elements) and the complete etching of the materials within the nano-grooves. Additionally, the distribution of I element at the nano-groove edges and the elemental content indicate significant depletion of I element (Supplementary Fig. 9), while no significant change in Nb and O element distribution is observed, especially no evidence of oxygen accumulation like oxidation behavior. This result rules out edge oxidation of the material and confirms the decomposition of the I element at the edges, transforming from $NbOI_2$ to NbO_x. X-ray photoelectron spectroscopy (XPS) was used to determine the valence state distribution of the amorphous NbO_X at the edges, as depicted in Supplementary Fig. 10. In the XPS spectrum of the Nb element in the original $NbOI_2$, peaks at 205.07 eV and 207.86 eV are observed, corresponding to the Nb $3d_{3/2}$ and Nb $3d_{5/2}$ peaks of Nb^{4+}. However, the XPS spectrum of the Nb element in the NGA structure revealed two new peaks at 207.04 eV and 209.89 eV, corresponding to the Nb $3d_{3/2}$ and Nb $3d_{5/2}$ peaks of Nb^{5+} [29]. Meanwhile, no peak differences are observed in the I element spectrum. Combining EDX and XPS characterizations, the presence of Nb_2O_5 components in the edge of NGA structures is confirmed. As described above, TEM characterization clearly demonstrates that fs laser-induced NGA structures retain the overall single crystal of $NbOI_2$, contrasting with the destructive characteristics of traditional LIPSS on materials. Notably, the nano-groove structures based on $NbOI_2$ exhibit an amorphous Nb_2O_5 layer at the edges as thin as a few nanometers, highlighting the “cold” cutting feature of fs laser processing on materials. Therefore, compared to the previously reported nano-patterning methods such as FIB, EBL combined with ion etching, and fs laser far-field processing not only offers advantages such as rapid, efficient, and flexible operation, but also preserves low-damage processing characteristics, providing a foundation for the development of high-performance electronic devices.

Generation mechanism of nano-groove array structures

Then, we intend to analyze the generation mechanism of fs laser-induced super-resolution NGA structures. The formation of super-

https://doi.org/10.1038/s41467-025-59520-9

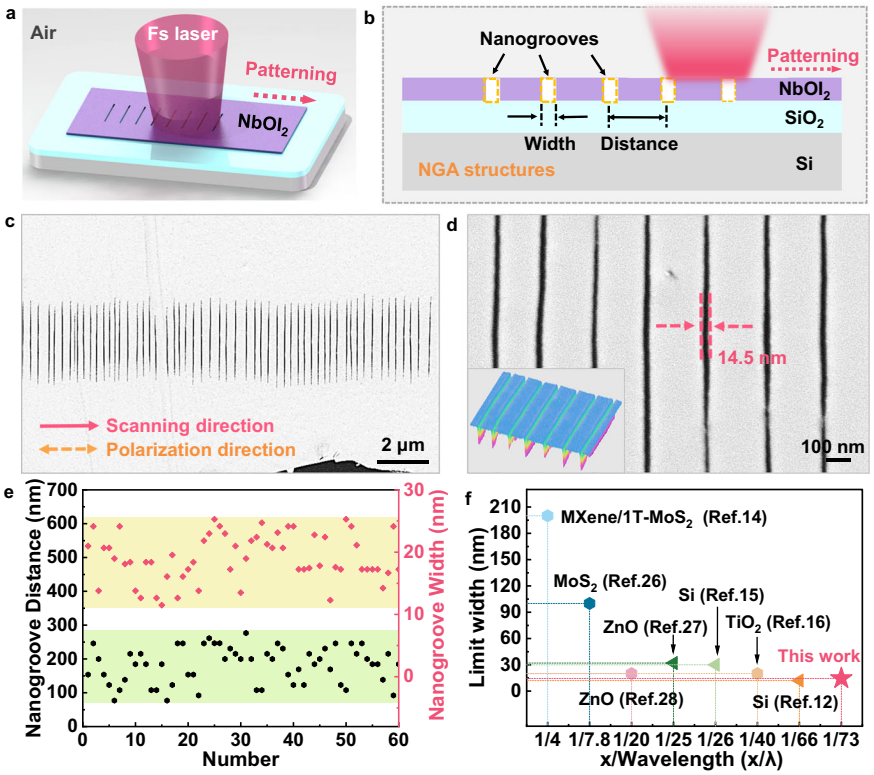

Fig. 1 | Preparation of fs laser-induced super-resolution nano-groove array (NGA) structures in 2D $NbOI_2$. **a** Schematic illustration of fs laser-induced NGA structure generation. **b** Structural schematic of super-resolution NGA structures. The 2D multilayer $NbOI_2$ nanosheets were transferred onto a silicon dioxide substrate, followed by scanning with a focused Gaussian beam of an fs laser, generating NGA structures in the laser-scanned area. **c** SEM image of super-resolution NGA structures. The experiment was repeated three times independently with similar results. **d** Magnified SEM image of the structure in (**c**), with an inset of a pseudo-color 3D image. **e** Statistics of average nano-groove distance and width. **f** Comparison of nano-groove widths with the representative laser-induced nanostructures. The horizontal axis represents the resolution-to-wavelength ratio (x/λ), while the vertical axis indicates the minimum processing width. Source data are provided as a Source Data file.

regular NGA structures induced by single-beam laser irradiation is an intriguing phenomenon. LIPSS are classified into low spatial frequency LIPSS (LSFLs, with a period >0.5λ) and high spatial frequency LIPSS (HSFLs, with a period <0.5λ)[18]. It is evident that the super-resolution NGA structures induced by a 1064 nm fs laser on $NbOI_2$ nanosheets are typical HSFLs. Several possible models have been proposed to explain the mechanism of HSFLs, including nanoplasmonic enhancement models[18,30], SHG induction[31], and self-organization mechanisms[32]. The occurrence of SHG typically results in structural orientations that are independent of the laser polarization direction. However, the consistent perpendicular alignment of the NGA structures to the laser polarization direction rules out the possibility of an SHG mechanism. The phenomenon of self-organization arises from surface undulations caused by non-equilibrium defects in the material. The intact single-crystal structure and smooth surface of the non-ablated regions in the NGA structures further exclude the occurrence of self-organization. Regarding the generation mechanism of the NGA structures, we propose a modified nanoplasmonic enhancement mechanism based on the interaction of nano-groove-induced local near-field (NG-LNF) coupling with the surface plasmon polariton (SPP) periodic field. As shown in Fig. 3a and Supplementary Fig. 11, this mechanism consists of three main processes: (i) the generation of laser-induced nanoplasma, which excites the SPP periodic field, (ii) the enhancement of the NG-LNF, and (iii) the coupling of the SPP field and NG-LNF.

Under the irradiation of an fs laser, a large number of free electrons are generated at the material's surface, resulting in the eruption of plasma. The influence of the plasma causes a change in the material's dielectric constant, inducing the formation of a periodic SPP field (Supplementary II-1). Supplementary Figs. 13 and 14 illustrate the changes in free electron density, dielectric constant, and surface temperature distribution. It is evident that under the influence of the periodic temperature field, when the temperature exceeds the material's ablation point (T_a), selective periodic ablation will occur (Supplementary Fig. 14). Additionally, we introduced a variable pulse number to alter electron density and conducted non-in situ experimental observations of structural evolution. As illustrated in Fig. 3b and Supplementary Fig. 15, variations in the number of pulses (N) affect the number of nano-grooves. At $N = 60$, a nano seed is generated at the Gaussian beam center, which grows into a nano-groove along a direction perpendicular to the direction of laser polarization. The finite-difference time-domain (FDTD) method is employed to simulate the electric field distribution at the interface when incident light interacts with the nano seed. Supplementary Fig. 16 confirms the electrical field-enhanced phenomenon at both ends of the nano-groove under the polarized light field, explaining the growth mechanism of the nano-groove. As the number of pulses increases, the number of nano-grooves gradually rises to 3, 4, and 6 roots until saturation is reached. It is noteworthy that, normally, a stronger energy at the Gaussian beam center would promote an increase in periodicity (Supplementary II-1 Equations (1–6)). However, the periodic distribution of the nano-grooves along the Gaussian beam, characterized by a smaller period in the center and a larger period on the sides, contradicts traditional SPP theoretical models.

Under the excitation of light fields, nano-grooves will induce LNF effects[33,34] (Supplementary II-2). To verify the existence of NG-LNF, the FDTD simulates the electric field distribution at the interface when incident light interacts with the nano-grooves. As illustrated in Fig. 3c, d, and Supplementary Fig. 17, it can be predicted that when

https://doi.org/10.1038/s41467-025-59520-9

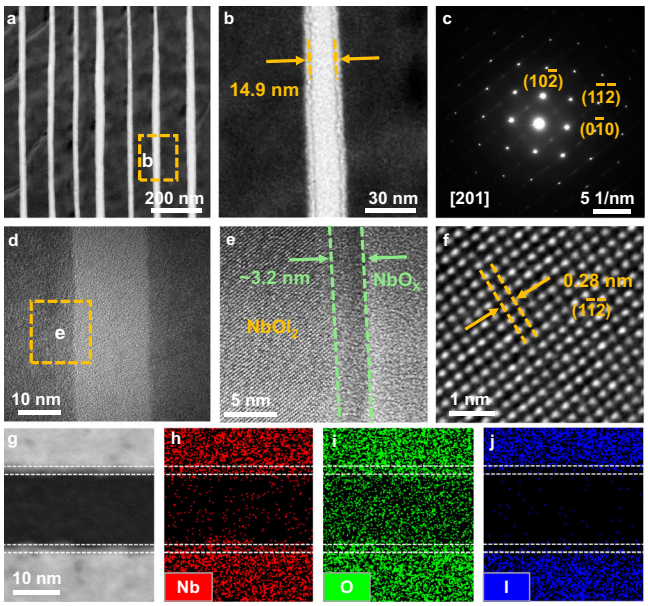

Fig. 2 | TEM characterization of fs laser-induced super-resolution NGA structures in 2D $NbOI_2$. **a** Low-magnification image of the NGA structures. **b** Low-magnification image of a single nano-groove. The experiments of (**a**–**c**) were repeated three times independently with similar results. **c** SAED of (**b**). **d** HRTEM image of the NGA structure. **e** Edge magnification of HRTEM from (**d**). **f** HRTEM image of the $NbOI_2$ regions out of nano-grooves. The experiments of (**d**–**f**) were repeated three times independently with similar results. **g**–**j** Elemental analysis of nano-grooves.

multiple pre-fabricated nano-grooves are induced by the periodic SPP field, an LNF effect will occur between every two nano-grooves under fs laser irradiation, leading to the secondary splitting of the nanostructures. Increasing the laser energy will promote the occurrence of LNF, which explains why the regions with higher energy at the center of the Gaussian beam exhibit smaller periodicity. To confirm the occurrence of the coupling field of the SPP field and NG-LNF, we conducted quasi in situ experiments on the evolution of the NGA structures. First, an initial NGA structure with relatively large spacing was induced using a low laser fluence of 22.75 mJ·cm^{-2}, during which SPP played a crucial role in its formation. Next, the fluence was increased to 32.5 mJ·cm^{-2}, and the same region was scanned again to observe the differences between the secondary structure and the initial structure. The experimental results, as shown in Fig. 3e, f and Supplementary Fig. 18, demonstrate that secondary structures are successfully induced at higher laser fluence. A comparison between the primary and secondary structures reveals that the secondary structures arise from the division of the primary structures, validating the effectiveness of the SPP-LNF coupled field mechanism.

Tunability of nano-groove array structures

Next, the tunable characteristics of NGA structures were investigated. The fluence of a pulsed laser is a critical parameter, representing the energy per unit area of a single pulse. As discussed in Supplementary II-1, changes in laser fluence affect the density of free electrons and the intensity of plasma, which further leads to variations in the dielectric constant of the material. According to the traditional SPP theory, an increase in laser fluence will result in a periodic increase. However, in the case of the SPP-LNF coupled field, under higher fluence, the LNF enhancement between NGA structures becomes intense, causing secondary splitting in the structure (Fig. 3f), which ultimately dominates and leads to an overall reduction in periodicity. To verify this hypothesis, NGA structures under different laser fluences are shown in Fig. 4a, indicating that the average spacing of nanostructures gradually decreases with increasing laser fluences, confirming the possibility of modulating the average period of nanostructures with laser fluences. Figure 4b provides statistics on the average spacing under different laser fluences, suggesting that further decreases in laser fluences may lead to controllable preparation of single nano-groove structures. As illustrated in the inset image of Fig. 4b, the generation of a single nano-groove did occur in our experiments. However, due to the sensitivity of single nano-grooves to laser parameters, controlled fabrication of the nanostructure is currently unattainable. Raman spectra of nanostructures in Fig. 4c confirmed their structural integrity, with a gradual attenuation of Raman peak intensity from $NbOI_2$ and a simultaneous enhancement of the silicon substrate's signal.

Additionally, an increase in the number of pulses can enhance the free electron density through accumulation, thereby affecting the periodicity of the NGA structure. Thus, it has been demonstrated that adjusting the scan speed can also be used to control the periodicity of the NGA structure (Supplementary Fig. 20). Figure 4a and Supplementary Fig. 20 illustrate the longitudinal expansion of the NGA structure's dimensions as laser fluence increases or the number of pulses rises. This expansion results from the increase in the effective ablation radius caused by the Gaussian beam (see Supplementary III-1(1)). The modulation of structure by laser wavelength is also discussed in Supplementary III-1(2). Due to its higher photon energy, the 532 nm laser induces a shift in the photoionization mode to single-photon absorption, resulting in a reduced structural period, decreased regularity, and severe ablation (Supplementary Fig. 21).

The controllability of nanostructure orientation was also investigated. By adjusting the half-wave plate in the optical system, controlled modulation of laser polarization direction is achieved. Due to the perpendicular relationship between nanostructures and polarization direction, good control of NGA structure orientation can be achieved with modulation of polarization direction (Supplementary Fig. 22). However, due to the unique stacking pattern of the nano-grooves resulting from the angle between the scanning direction and the laser polarization direction, the best structural regularity and fabrication quality are achieved when the laser scanning direction aligns at 0 degrees with the polarization direction (Supplementary Fig. 23). Moreover, by changing the laser scanning trajectory, it can be observed that the orientation of nanostructures remains perpendicular to the laser polarization direction, regardless of the laser scanning direction (Supplementary Fig. 24). The influence of laser scanning times on the NGA structures indicates that the number of laser scanning times does not induce recombination of nanostructures (Supplementary Fig. 25).

Nanopatterning is crucial for the application of nanostructures in electronic devices. To demonstrate the flexibility of laser processing, exploration of NGA structure patterning based on 2D $NbOI_2$ was conducted. Figure 4d and Supplementary Fig. 26 present the writing of the pattern "HIT", with a scanning speed set at 0.01 mm/s. The writing time for this pattern was only 10 s, and the nanostructures were intact with good structural alignment. This showcases the rapidity and flexibility of fs laser-induced nanostructure patterning. With the advancement of material synthesis techniques, achieving large-scale nano-patterning fabrication of $NbOI_2$ materials holds significant promise. In addition, to validate the general applicability of the method proposed in this study, NGA structure preparation experiments were conducted on other 2D $NbOX_2$ materials (NbOBrI and $NbOCl_2$) as well as transition metal dichalcogenides materials (2H-WS_2 and 3R-MoS_2) (Supplementary Fig. 27). Similar NGA structures were observed on NbOBrI, 2H-WS_2, and 3R-MoS_2. However, there are some differences in the structural regularity and surface quality across the various materials. These differences are closely related to the periodic temperature field

https://doi.org/10.1038/s41467-025-59520-9

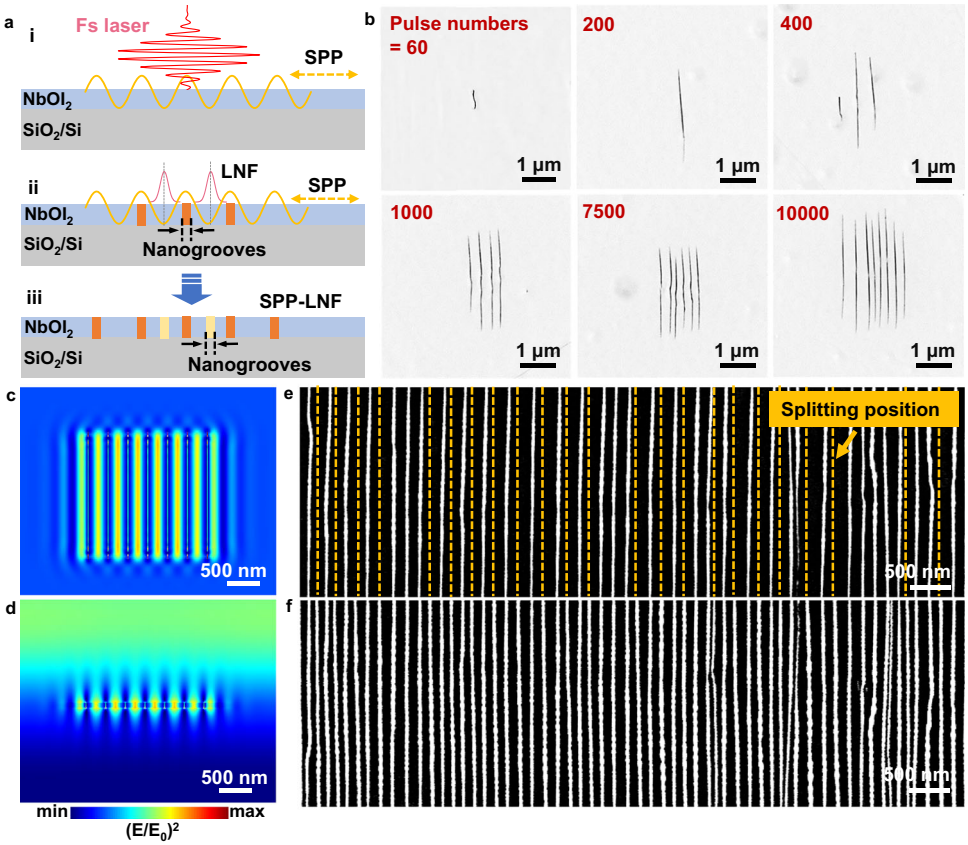

Fig. 3 | The generation mechanism of fs laser-induced super-resolution nano-groove array structures (NGA). a A coupled field model based on the interaction between the surface plasmon polariton (SPP) periodic field and the nano-groove-induced local near-field (NG-LNF). This model consists of three main processes: (i) the generation of laser-induced nanoplasma, which excites the SPP periodic field, (ii) the enhancement of the NG-LNF, and (iii) the coupling of the SPP field and NG-LNF. **b** Structure evolution induced by multi-laser pulse excitation. **c**, **d** Electric field distribution on the XY plane and the YZ plane. FDTD numerical simulation exhibits a secondary splitting mechanism induced by the NGA structure. **e**, **f** Quasi in situ observation of the secondary evolution of NGA structures. **e** The grayscale SEM image of NGA structure after the first scan under a laser fluence of 22.75 mJ cm^{-2}. **f** The grayscale SEM image of NGA structure after the second scan under a laser fluence of 32.5 mJ cm^{-2}. To facilitate a clearer comparison, the image (**f**) was vertically flipped. The experiments of (**e**, **f**) were repeated three times independently with similar results. Source data are provided as a Source Data file.

gradient induced by laser irradiation, the excitation intensity of the LNF, and the intrinsic properties of the materials, such as absorption, thermal conductivity, and their melting, evaporation, or oxidation temperatures. Supplementary III-4 systematically analyzes the potential impacts of material properties like absorption coefficient, thermal conductivity, and oxidation temperature on the resulting structures.

Therefore, the use of the SPP-LNF mechanism for fs laser processing enables the fabrication of NGA structures, offering advantages such as super-resolution, low structural damage, structural tunability, and large-area patterning. This method has also been proven to be applicable to 2D materials like 2H-WS_2 and 3R-MoS_2. However, due to factors such as the single form of the optical field and differences in material properties, the current processed structures are limited to grooves, and there are variations in the regularity of structures when processed on different 2D materials. Therefore, further refinement of the SPP-LNF method will be necessary in the future, through optical field modulation and material property simulations, with the goal of achieving broader structural processing capabilities and enhancing the method's applicability.

Nano-groove array-$NbOI_2$ gas sensor

The NGA structure possesses super-resolution structural dimensions and preserves the single-crystalline nature of $NbOI_2$ while simultaneously offering a substantial increase in heterojunctions between $NbOI_2$ and the amorphous Nb_2O_5 edges. In contrast to traditional methods of fabricating heterostructures, the fs laser processing technique provides the advantage of high efficiency and flexible patterning, granting NGA structures significant potential for device applications. Furthermore, Nb_2O_5, widely recognized as an effective material for heterojunction charge transfer[29], has attracted significant interest in fields such as photocatalysis[35]. Differential charge density calculations (Supplementary Fig. 28) confirm substantial charge transfer at the $NbOI_2$-Nb_2O_5 interface, and this redistribution of interfacial charge is often expected to create numerous active sites for gas molecule adsorption, thereby enhancing gas-sensing capabilities. Therefore, the gas-sensing performance of the $NbOI_2$ device based on fs laser-induced NGA structures with a large amount of amorphous Nb_2O_5 edges was investigated. The schematic diagram of the device is shown in Fig. 5a. 2D $NbOI_2$ nanosheets with super-resolution NGA structures were used as sensing media. To ensure the conductivity of the device, the nanostructure direction was aligned parallel to the two end electrodes. The gas-sensing sensor operating current was set to +5 V, and it was exposed to NO_2 gas. The definitions of gas sensor responses, response, and recovery time are described in the "Method" section.

Firstly, to confirm the difference in gas-sensing performance between 2D $NbOI_2$ devices with (NGA-$NbOI_2$ sensor) and without NGA

https://doi.org/10.1038/s41467-025-59520-9

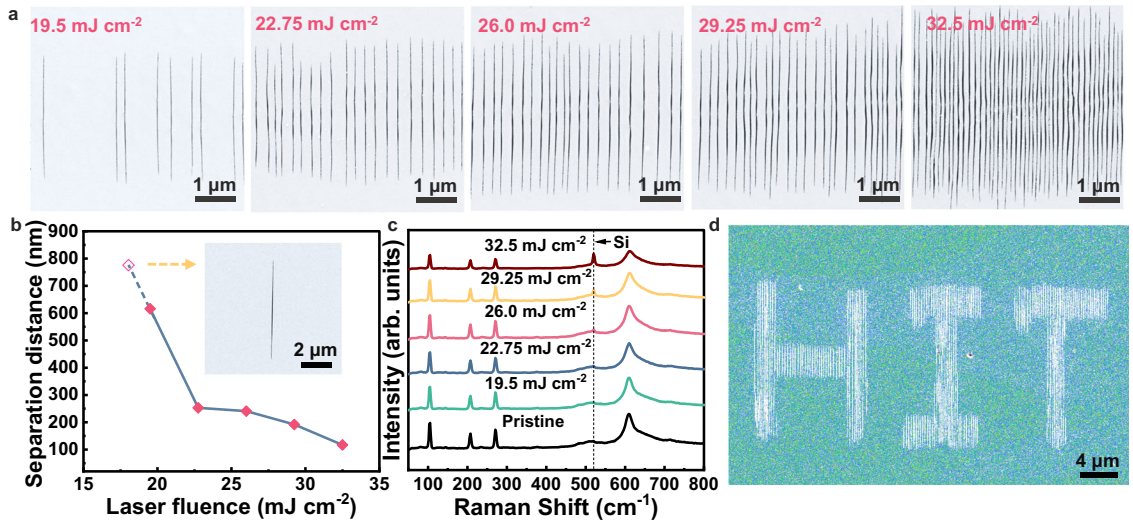

Fig. 4 | Tunability of nano-groove array structures. a Influence of laser fluence on the structures. **b** Variation law of nanoscale spacing under the action of laser fluence. The inset illustrates the preparation of a single nano-groove. **c** Raman spectra at different laser fluences in (**a**). **d** Writing of "HIT" pattern. "HIT" is the abbreviation for Harbin Institute of Technology. Source data are provided as a Source Data file.

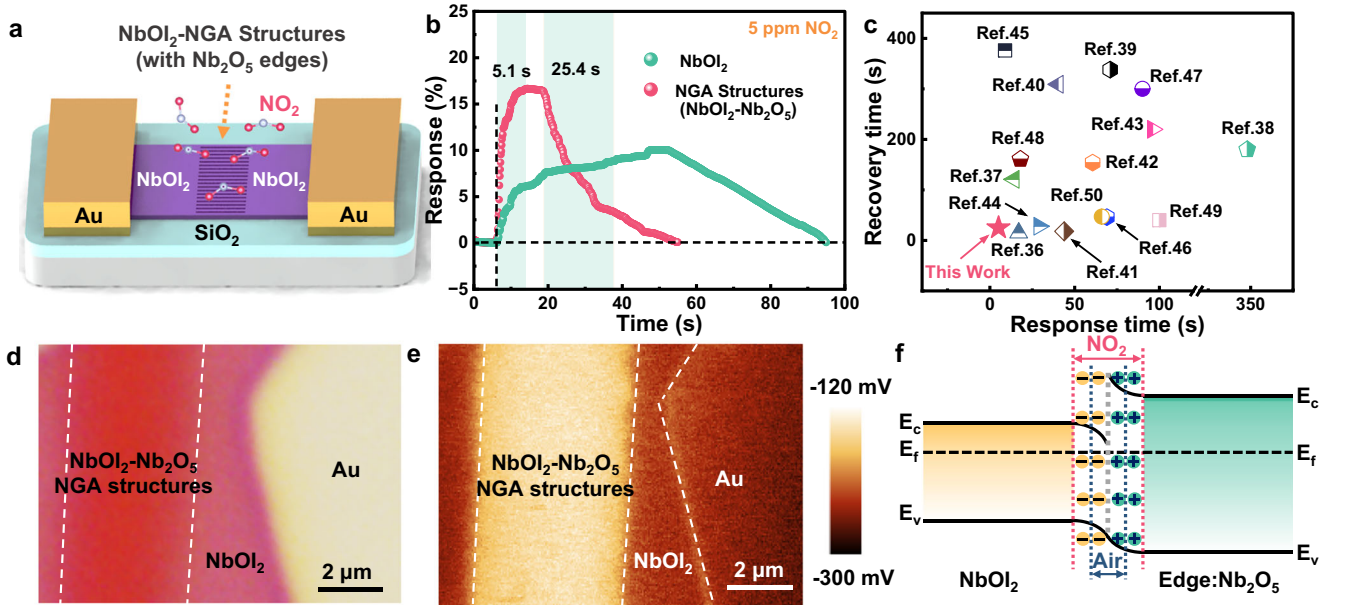

Fig. 5 | Gas-sensing performance of the nano-groove array-$NbOI_2$ (NGA-$NbOI_2$) gas sensor. a Schematic diagram of the NGA-$NbOI_2$ gas sensor. **b** Performance comparison of gas sensors with or without NGA structures under the action of 5 ppm NO_2 gas. The left green shadow represents the gas response stage, and the right green shadow represents the gas recovery stage. **c** Response-recovery time (operating temperature: 25 °C) of this work compared with previous works[36–50] in recent years. **d** Optical image of 2D $NbOI_2$ nanosheet with NGA structures on a gold substrate. **e** Surface potential mapping of the area in Fig. 5d using KPFM. **f** Energy band structure of $NbOI_2$-edge Nb_2O_5 heterostructures in air and NO_2 atmosphere. E_c, E_v, and E_f represent the conduction band, valence band, and Fermi level positions of the material, respectively. Source data are provided as a Source Data file.

structures, comparative tests were conducted. As presented in Fig. 5b, the results indicate that the NGA-$NbOI_2$ sensor has a high response value of up to 16.5% at room temperature when exposed to a 5 ppm concentration of NO_2 gas, with a rapid response time of 5.1 s and a recovery time of 25.4 s. However, the original $NbOI_2$ devices without the NGA structure exhibited a response value of only 10.14%, a response time of 26.5 s, and a recovery time of 57.6 s. This clearly demonstrates the crucial role of the NGA structure in enhancing device performance. A statistical analysis of the response and recovery time of gas sensors from recent years, as shown in Supplementary Table 3 and Fig. 5c[36–50], reveals that the NGA-$NbOI_2$ sensor exhibits an exceptionally fast response speed for NO_2 detection, laying the foundation for fast gas-sensing applications for NO_2. In addition, a comprehensive characterization of the gas-sensing performance on the NGA-$NbOI_2$ sensor was conducted (Supplementary Fig. 29). The NGA-$NbOI_2$ sensor exhibited excellent detection stability and good gas selectivity for NO_2. Additionally, it can detect NO_2 concentrations ranging from 0.5 to 70 ppm in dry air at room temperature. To verify the gas-sensing performance of the NGA-$NbOI_2$ sensor across different environments, we conducted gas-sensitivity tests under varying temperature and humidity conditions (Supplementary Figs. 30 and 31) as well as long-term stability tests of the device (Supplementary

Figs. 32 and 33). The results confirmed the sensor's reliable stability in different environments.

Finally, the mechanism behind the enhanced gas-sensing performance of the NGA-$NbOI_2$ sensor was investigated. As previously discussed, the abundant $NbOI_2$-Nb_2O_5 interfaces and substantial charge transfer play a crucial role in enhancing gas-sensing performance. As illustrated in Supplementary Figs. 34–36, the poor conductivity of Nb_2O_5 and its insensitivity to NO_2 indicate that it does not contribute to the enhancement of gas-sensing performance. Therefore, the results indicate that the performance improvement is directly related to the presence of abundant heterojunctions between $NbOI_2$ and the amorphous Nb_2O_5 edges. By measuring the local surface potential by Kelvin probe force microscopy (KPFM) in Fig. 5d, e, it can be seen that the surface potential in the NGA structure regions is significantly higher than that in the $NbOI_2$ regions. The work functions and Fermi level positions of the $NbOI_2$ and NGA structures were determined to be 5.08 eV and 4.89 eV, respectively (Supplementary Fig. 37), indicating that the Fermi level of the $NbOI_2$-Nb_2O_5 heterojunction is lower than that of $NbOI_2$. This suggests that the Fermi level of intrinsic $NbOI_2$ is higher than that of the amorphous Nb_2O_5 edges. Therefore, upon the formation of the heterojunction structure, electrons will transfer from the amorphous Nb_2O_5 edges to the $NbOI_2$ region until Fermi energy equilibrium is reached (Fig. 5f). Once the heterojunction is formed, an internal potential will be generated. During the sensing process, adsorbed NO_2 molecules will capture electrons from the heterojunction, further increasing the barrier width, thereby reducing the conductivity of the NGA-$NbOI_2$ sensors and resulting in a rapid sensing response.

In summary, we demonstrated that far-field fs laser patterning can be employed to fabricate NGA structures with groove widths as low as ~14.5 nm (~λ/73), and NGA structures exhibit a smooth surface without obvious ablation. Through structural characterization, it has been validated that the NGA structures retain the original single-crystalline nature of $NbOI_2$ and exhibit ultrafine amorphous Nb_2O_5 edges, thus affirming the advanced processing capability of selectively etching 2D multilayer $NbOI_2$ using the LIPSS method. Through numerical simulations and experimental studies, it has been demonstrated that the generation of NGA structures originates from the coupled field of SPP periodic field and NG-LNF enhancement induced by fs laser irradiation. Furthermore, by adjusting laser parameters such as laser pulse number, fluence, and polarization direction, the groove spacing, quantity, and orientation of NGA structures can be modulated. Finally, based on the large number of $NbOI_2$-Nb_2O_5 heterojunctions generated by the NGA structure and the significant charge transfer occurring at their interfaces, NGA-$NbOI_2$ gas sensors were fabricated, demonstrating highly competitive NO_2 sensing performance with a rapid response time (~5.1 s) and a quick recovery time (25.4 s). Leveraging the super-resolution capability of laser patterning, the richness of the $NbOI_2$-Nb_2O_5 heterojunction, and the nonlinear optical characteristics of $NbOI_2$ itself, the NGA structure is expected to play a greater role in future catalysis, molecular sensing, and nanophotonics.

Methods

Materials preparation

$NbOI_2$ single-crystal bulk materials were synthesized using the chemical vapor transport (CVT) technique. In a vacuum-sealed quartz tube, powders of Nb, Nb_2O_5, and I_2 were uniformly mixed in a ratio of 3:1:6. The tube was programmatically heated to 700 °C, held at this temperature for 3 hours, and then allowed to cool naturally to room temperature. To eliminate residual I_2, the obtained crystals were immersed in alcohol. Thin $NbOI_2$ flakes were obtained through mechanical exfoliation on polydimethylsiloxane. Subsequently, these flakes were transferred onto a 10 × 10 mm SiO_2/Si substrate using a dry transfer method.

Femtosecond laser processing

The sample is placed on an electrically controlled three-axis sample stage, subsequently laser-patterned in air. The fs laser has a wavelength of 1064 nm, a pulse width of 255 fs, and exhibits a Gaussian beam profile. The laser output is linearly polarized light, attenuated in power through a half-wave plate and a Glan prism, and further adjusted in polarization direction via another half-wave plate. Upon focusing through the objective lens, a spot size of approximately 10 μm can be achieved. The scanning speed of the processing platform is set to 0.01 mm/s, with the capability to achieve different laser scanning trajectories through software configuration.

Numerical simulation

The finite-difference time-domain (FDTD) method is used to simulate the interface electric field distribution when incident light interacts with the nano-grooves. The computational model consists of Si, SiO_2, and $NbOI_2$ materials from bottom to top, with dimensions of 5 μm × 5 μm in length and width, and heights of 2 μm, 300 nm, and 10 nm, respectively. The simulation region is a rectangular box with dimensions of 4 μm × 4 μm × 4.8 μm. Symmetric periodic boundary conditions were applied along the X and Y axes. A plane wave with a wavelength of 1064 nm was set as the incident light, irradiating from a distance of 1 μm above the surface of the $NbOI_2$ material. Seven nano-grooves with dimensions of 2 μm × 15 nm × 10 nm were created, and a plane wave with a wavelength of 1064 nm was applied to irradiate the grooves.

Materials characterization

The optical images of 2D $NbOI_2$ were obtained using an optical microscope (Zeiss Imager A2m). The NGA structures of 2D $NbOI_2$ were characterized using a scanning electron microscope (SEM, Zeiss Sigma 300 VP), and image processing was performed using Gwyddion software. The transmission electron microscope (TEM, Talos F200x) was utilized to analyze the atomic structure distribution and employed selected area electron diffraction (SAED) imaging, while energy-dispersive X-ray spectroscopy (EDX) was employed to determine the elemental distribution of the structure. Raman spectra characterization of the $NbOI_2$ samples was conducted using a micro-Raman system (Renishaw InVia Plus) equipped with a 532 nm excitation laser and a 50× objective. The Raman power was set at 5%, and a data acquisition time of 5 s was used. Second harmonic generation (SHG) spectra were measured using a home-built setup with back-reflection configuration, employing an fs laser with a wavelength of 1064 nm and a pulse width of 80 fs. X-ray photoelectron spectroscopy (XPS, ESCALAB 250Xi, Al Kα radiation) was employed for the characterization of the material's valence states. Kelvin probe force microscopy (KPFM) measurements were performed in tapping mode using an atomic force microscope (AFM, Bruker Dimension FastScan) to measure the surface potential distribution of the structures.

Gas-sensing measurement

SiO_2/Si chip carriers were prepared using ultraviolet exposure techniques, and electrical measurements were conducted using a 2/40 nm Cr/Au film deposited by thermal vacuum evaporation. The chip contained electrode channels of 10 μm, and external electrodes of 3 mm were directly connected to the probe clamp. 2D $NbOI_2$ nanosheets were transferred into the channels, followed by nanofabrication using an fs laser. The NO_2 sensing experiments were performed in a custom-designed gas-sensing chamber equipped with gas inlet and outlet devices, as well as electrode contacts for detection. Real-time changes in conductivity were observed and recorded at a voltage of 5 V using an electrochemical workstation (CHI 630E). The background gas consisted of air, and a predetermined quantity of target gas (1 L) was introduced into the testing chamber using a syringe. Gas sensor sensitivity can be expressed using the following Equations: S (%) = [(I_a/

$I_g) - 1] \times 100\%$ for reducing gases, and $S\ (\%) = [(I_g/I_a) - 1] \times 100\%$ for oxidizing gases. Here, I_a represents the drain current in air, while I_g represents the drain current when the sensor is exposed to the gas being tested. Response time is defined as the time needed to achieve 90% of the change in the gas response sensitivity when the sensor is exposed to a specific amount of gas, and recovery time is defined as the time needed for gas desorption to restore 90% of the initial signal after cutting off the gas.

Reporting summary

Further information on research design is available in the Nature Portfolio Reporting Summary linked to this article.

Data availability

The data generated in this study are provided in the main text, supplementary information, and source data file. Additional data are available from the corresponding author on request. Source data are provided with this paper.

References

1. Rahman, S. & Lu, Y. Nano-engineering and nano-manufacturing in 2D materials: marvels of nanotechnology. *Nanoscale Horiz.* **7**, 849–872 (2022).
2. Yin, L. et al. Two-dimensional semiconductors and transistors for future integrated circuits. *ACS Nano* **18**, 7739–7768 (2024).
3. Wang, Z. et al. Exciton-enabled meta-optics in two-dimensional transition metal dichalcogenides. *Nano Lett.* **20**, 7964–7972 (2020).
4. Liu, X., Ma, T., Pinna, N. & Zhang, J. Two-dimensional nanostructured materials for gas sensing. *Adv. Funct. Mater.* **27**, 1702168 (2017).
5. Wu, X. et al. Emerging 2D materials for electrocatalytic applications: synthesis, multifaceted nanostructures, and catalytic center design. *Small* **18**, 2105831 (2022).
6. Liu, S. et al. Nanopatterning technologies of 2D materials for integrated electronic and optoelectronic devices. *Adv. Mater.* **34**, 2200734 (2022).
7. Haas, J. et al. Aligned stacking of nanopatterned 2D materials for high-resolution 3D device fabrication. *ACS Nano* **16**, 1836–1846 (2022).
8. Bell, D. C., Lemme, M. C., Stern, L. A., Williams, J. R. & Marcus, C. M. Precision cutting and patterning of graphene with helium ions. *Nanotechnology* **20**, 455301 (2009).
9. Fox, D. S. et al. Nanopatterning and electrical tuning of MoS_2 layers with a subnanometer helium ion beam. *Nano Lett.* **15**, 5307–5313 (2015).
10. Zheng, F. et al. Sub-nanometer electron beam phase patterning in 2D materials. *Adv. Sci.* **9**, 2200702 (2022).
11. Rani, E. & Wong, L. S. High-resolution scanning probe nanolithography of 2D materials: novel nanostructures. *Adv. Mater. Technol.* **4**, 1900181 (2019).
12. Lin, Z., Liu, H., Ji, L., Lin, W. & Hong, M. Realization of ~10 nm features on semiconductor surfaces via femtosecond laser direct patterning in far field and in ambient air. *Nano Lett.* **20**, 4947–4952 (2020).
13. Kadoguchi, N. et al. Nanoprocessing of self-suspended monolayer graphene and defect formation by femtosecond-laser irradiation. *Nano Lett.* **23**, 4893–4900 (2023).
14. Yuan, Y. et al. Laser maskless fast patterning for multitype microsupercapacitors. *Nat. Commun.* **14**, 3967 (2023).
15. Lin, Z., Ji, L. & Hong, M. Approximately 30 nm nanogroove formation on single crystalline silicon surface under pulsed nanosecond laser irradiation. *Nano Lett.* **22**, 7005–7010 (2022).
16. Li, Z.-Z. et al. O-FIB: far-field-induced near-field breakdown for direct nanowriting in an atmospheric environment. *Light Sci. Appl.* **9**, 41 (2020).
17. Zhang, Y. et al. Femtosecond laser-induced periodic structures: mechanisms, techniques, and applications. *OES* **1**, 220005–220005 (2022).
18. Bonse, J. & Gräf, S. Maxwell meets Marangoni—a review of theories on laser-induced periodic surface structures. *Laser Photonics Rev.* **14**, 2000215 (2020).
19. Zuo, P. et al. Maskless micro/nanopatterning and bipolar electrical rectification of MoS_2 flakes through femtosecond laser direct writing. *ACS Appl. Mater. Interfaces* **11**, 39334–39341 (2019).
20. Kim, Y.-J. et al. Tailoring two-dimensional matter using strong light–matter interactions. *Nano Lett.* **23**, 3645–3652 (2023).
21. Abdelwahab, I. et al. Giant second-harmonic generation in ferroelectric $NbOI_2$. *Nat. Photon.* **16**, 644–650 (2022).
22. Guo, Q. et al. Ultrathin quantum light source with van der Waals $NbOCl_2$ crystal. *Nature* **613**, 53–59 (2023).
23. Liu, C. et al. Ferroelectricity in niobium oxide dihalides $NbOX_2$ (X = Cl, I): a macroscopic- to microscopic-scale study. *ACS Nano* **17**, 7170–7179 (2023).
24. Fu, J. et al. Emission dipole and pressure-driven tunability of second harmonic generation in vdWs ferroelectric $NbOI_2$. *Adv. Funct. Mater.* https://doi.org/10.1002/adfm.202308207 (2023).
25. Sun, X., Wan, Y., Fang, Y. & Huang, F. Layered ferroelectric $NbOI_2$ flakes toward in-plane anisotropic self-powered sensing. *Small Sci.* **4**, 2300125 (2024).
26. Enrico, A. et al. Ultrafast and resist-free nanopatterning of 2D materials by femtosecond laser irradiation. *ACS Nano* **17**, 8041–8052 (2023).
27. Liu, J. et al. Direct writing of 150 nm gratings and squares on ZnO crystal in water by using 800 nm femtosecond laser. *Opt. Express* **22**, 32361 (2014).
28. Bai, S., Li, Z., Obata, K., Kawabata, S. & Sugioka, K. λ /20 surface nanostructuring of ZnO by mask-less ultrafast laser processing. *Nanophotonics* **12**, 1499–1510 (2023).
29. Huang, X. L. et al. Orthorhombic Nb_2O_5 decorated carbon nanoreactors enable bidirectionally regulated redox behaviors in room-temperature Na–S batteries. *Adv. Sci.* **10**, 2206558 (2023).
30. Bhardwaj, V. R. et al. Optically produced arrays of planar nanostructures inside fused silica. *Phys. Rev. Lett.* **96**, 057404 (2006).
31. Jia, T. Q. et al. Formation of nanogratings on the surface of a ZnSe crystal irradiated by femtosecond laser pulses. *Phys. Rev. B* **72**, 125429 (2005).
32. Reif, J., Varlamova, O., Uhlig, S., Varlamov, S. & Bestehorn, M. On the physics of self-organized nanostructure formation upon femtosecond laser ablation. *Appl. Phys. A* **117**, 179–184 (2014).
33. Cheng, K. et al. Ultrafast dynamics of single-pulse femtosecond laser-induced periodic ripples on the surface of a gold film. *Phys. Rev. B* **98**, 184106 (2018).
34. Geng, J., Shi, L., Sun, X., Yan, W. & Qiu, M. Artificial seeds-regulated femtosecond laser plasmonic nanopatterning. *Laser Photonics Rev.* **16**, 2200232 (2022).
35. Deng, X. et al. Ultrafast electron transfer at the In_2O_3/Nb_2O_5 S-scheme interface for CO_2 photoreduction. *Nat. Commun.* **15**, 4807 (2024).
36. Li, Y. et al. Preparation of BiOI-functionalized ZnO nanorods for ppb-level NO_2 detection at room temperature. *ACS Sens.* **7**, 3915–3922 (2022).
37. Ou, Y. et al. Tandem electric-fields prolong energetic hot electrons lifetime for ultra-fast and stable NO_2 detection. *Adv. Mater.* **36**, 2403215 (2024).
38. Kim, S. et al. Aerosol-synthesized surfactant-free single-walled carbon nanotube-based NO_2 sensors: unprecedentedly high sensitivity and fast recovery. *Adv. Mater.* **36**, 2313830 (2024).
39. Park, S. et al. Dual-photosensitizer synergy empowers ambient light photoactivation of indium oxide for high-performance NO_2 sensing. *Adv. Mater.* https://doi.org/10.1002/adma.202313731 (2024).

40. Liang, Z. et al. A 2D-0D-2D sandwich heterostructure toward high-performance room-temperature gas sensing. *ACS Nano* **18**, 3669–3680 (2024).
41. Kumar, A. et al. Investigations of vacancy-assisted selective detection of NO_2 molecules in vertically aligned SnS_2. *ACS Sens.* **8**, 1357–1367 (2023).
42. Saggu, I. S. et al. Ultrasensitive room-temperature NO_2 detection using SnS_2 /MWCNT composites and accelerated recovery kinetics by UV activation. *ACS Sens.* **8**, 243–253 (2023).
43. Zhao, Q. et al. Edge-enriched $Mo_2TiC_2T_x$ /MoS_2 heterostructure with coupling interface for selective NO_2 monitoring. *Adv. Funct. Mater.* **32**, 2203528 (2022).
44. Kumar, R., Jenjeti, R. N. & Sampath, S. Two-dimensional, few-layer $MnPS_3$ for selective NO_2 gas sensing under ambient conditions. *ACS Sen.s* **5**, 404–411 (2020).
45. Geng, X. et al. Atomically dispersed Pb ionic sites in PbCdSe quantum dot gels enhance room-temperature NO_2 sensing. *Nat. Commun.* **12**, 4895 (2021).
46. Bian, W. et al. Fabrication and computational study of a chemiresistive NO_2 gas sensor based on the carbon dots-WO_3 heterostructure for operating below room temperature. *ACS Sens* **8**, 748–756 (2023).
47. Li, X. et al. Highly flexible all-inorganic nanofiber networks with stress-accommodating microstructure for light-activated wearable chemiresistive sensor. *Chem. Eng. J.* **455**, 140768 (2023).
48. Zhang, L. et al. Rolling up of 2D nanosheets into 1D nanoscrolls: visible-light-activated chemiresistors based on surface modified indium selenide with enhanced sensitivity and stability. *Chem. Eng. J.* **446**, 136937 (2022).
49. Yang, B., Song, Y., Song, Y., Ma, Z. & Sun, J. TiO_2 QDs/$MoSe_2$ heterojunctions for enhanced photo-excited charge separation and gas sensing performance. *Sens. Actuators B Chem.* **379**, 133124 (2023).
50. Yueyue, L. et al. $CsPbBr_3$ quantum dots enhanced ZnO sensing to NO_2 at room temperature. *Sens. Actuators B Chem.* **368**, 132189 (2022).

Acknowledgements

The authors would like to thank Dr. Zhaoyuan Sun from the Center of Analysis and Measurement at Harbin Institute of Technology for SEM and KPFM measurements. This work was supported by National Key Research and Development Program of China (2023YFB4605102, Y.D., L.Y.), the National Natural Science Foundation of China (Nos. 52272146 (Y.L.), 51902069 (C.X., L.Z.), 52105437 (Y.D.), 61925304 (H.X.)), the Fundamental Research Funds for the Central Universities (Grant No. HIT.OCEF.2024001 (Y.L.)), Heilongjiang Touyan Team (No. HITTY-20190036 (Y.L.)), the Natural Science Foundation of Heilongjiang Province (No. YQ2021E019 (Y.L.)).

Author contributions

Y.G. and Y.D. contributed to this article equally. Y.G. and Y.L. proposed the research and designed the experiment; The experiments on materials preparation and characterizations were performed by Y.F., Y.D., Y.G., and R.W.; The mechanism of NGA structure analysis was performed by Y.G., J.L., and Y.N.L. Gas sensor measurement was supported by J.H. All authors participated in the discussion and analysis of results, and the manuscript was collaboratively written by Y.G. and Y.D.; L.Y., Y.L., C.X., H.X., and L.Z. provided support and supervision for the project.

Competing interests

The authors declare no competing interests.

Additional information

Supplementary information The online version contains supplementary material available at https://doi.org/10.1038/s41467-025-59520-9.

Correspondence and requests for materials should be addressed to Yuqiang Fang, Yang Li or Lijun Yang.

Peer review information *Nature Communications* thanks Jae-Young Choi, who co-authored with Hak Ki Yu, and Olivier Allegre for their contribution to the peer review of this work. A peer review file is available.